Research Article

Investigation of growth mechanism for highly oriented TiO_2 nanorods: the role of reaction time and annealing temperature

Bharat R. Bade[1,4] · Sachin Rondiya[2] · Somnath R. Bhopale[1] · Nelson Y. Dzade[2] · Mahesh M. Kamble[3] · Avinash Rokade[4] · Mamta P. Nasane[1] · Mahendra A. More[1] · Sandesh R. Jadkar[1] · Adinath M. Funde[4]

Abstract

Titanium dioxide (TiO_2) is a versatile and inexpensive material for extended applicability in several scientific and technological fields including photo-catalysis for industrial waste treatment, energy harvesting, and hydrogen production. In this work, we report the synthesis of TiO_2 thin film using hydrothermal method and investigations on the influence of reaction time and annealing temperature on growth mechanism of the TiO_2 nanorods. The synthesized TiO_2 films were studied by using UV–visible spectroscopy, Raman spectroscopy, X-ray diffraction (XRD), scanning electron microscope and energy-dispersive X-ray spectroscopy (EDS). The XRD and Raman measurements revealed the formation of defect free and pure tetragonal TiO_2 rutile phase. The TiO_2 thin films show absorption band edge at around 420 nm in the UV–visible spectrum and exhibit direct band gap value of 2.9 eV. The TiO_2 nanorods are demonstrated to grow randomly on the FTO substrate with changing reaction times but grow uniformly in a flower-like pattern with increasing annealing temperature. Investigation of the field emission properties of TiO_2 thin films (tested as field-emitter array) estimates the turn-on and threshold field at 4.06 and 7.06 V/μm at 10 and 100 μA/cm^2, respectively.

✉ Adinath M. Funde, adinathf@gmail.com | [1]Department of Physics, Savitribai Phule Pune University, Pune 411007, India. [2]The School of Chemistry, Cardiff University, Cardiff CF10 3AT, Wales, UK. [3]PDEA's Anantrao Pawar College, Pirangut, Mulshi, Pune 412115, India. [4]The School of Energy Studies, Savitribai Phule Pune University, Pune 411007, India.

SN Applied Sciences (2019) 1:1073 | https://doi.org/10.1007/s42452-019-0978-2

Received: 21 June 2019 / Accepted: 23 July 2019

Graphic Abstract

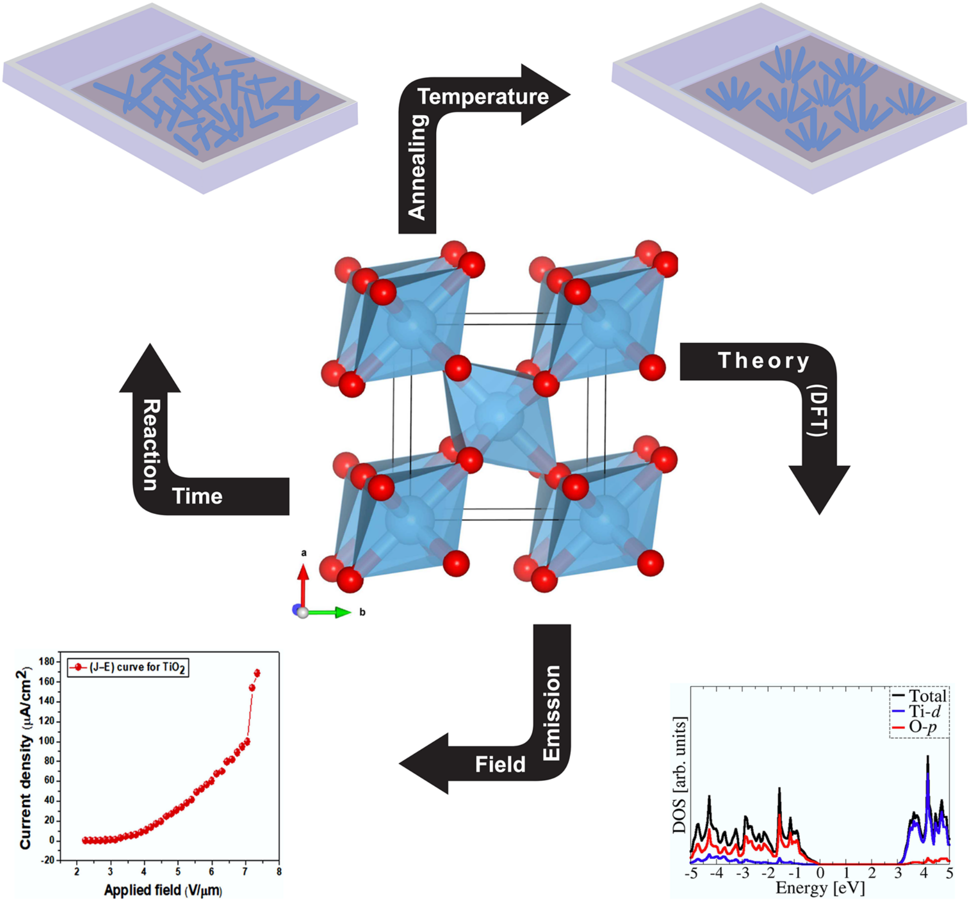

Keywords Titanium dioxide · Nanorods · Growth mechanism · Hydrothermal method · Density function theory · Field emission

1 Introduction

Nanocrystalline semiconductor materials have been attracting significant attention recently because of their unique physical and chemical properties that makes them attractive for application in industrial waste treatment (photocatalysis) and solar energy conversion (photovoltaics). Titanium dioxide (TiO_2) a wide bandgap material (3.4 eV) has emerged as the most studied of these photocatalysts owing to its high degradation efficiency with almost any organic molecule and many other attractive properties, including physical and chemical stability, low cost, good thin film transparency [1–5]. These germane properties make TiO_2 attractive materials for several applications including solar cell (DSSCs, QDSSCs, ETA Solar Cell) [6–10], photocatalysis [11], heterogeneous catalysis, environmental hazards removal [12], ceramics and paint industries [13–15], gas sensors [16, 17], and supercapacitors [18–20]. Besides, owing to its non-toxicity and biocompatibility, TiO_2 is found appropriate for application in cosmetics, food products, pharmaceuticals, and in the biomedical applications [13]. These applications of TiO_2 are mainly dependent on their crystalline structure, particle size, optical properties, and morphology [4, 21–23]. Thus, one of the important aspects of the development of TiO_2 nanoscience is our ability to control it size and morphology for specific applications such as e.g. photoconversion in solar cell and field emission arrays [24, 25]. Crystallographically, TiO_2 is naturally present in three phases, i.e. anatase, rutile, and brookite, with the rutile phase been the thermodynamically most stable phase. The anatase and rutile phase exhibit tetragonal crystalline structure, whereas the brookite phase has an orthorhombic structure [26, 27]. A variety of methods have been developed for the synthesis

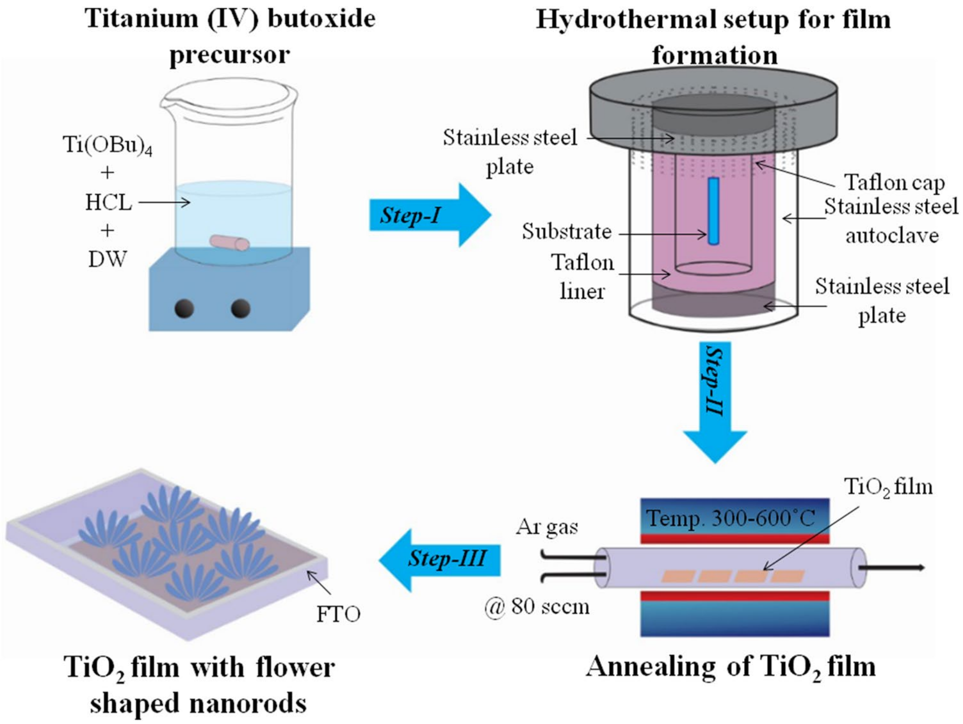

Fig. 1 Experimental setup of TiO_2 thin film formation using hydrothermal method

of TiO_2 nanoparticles with tailorable material properties like sol–gel [28–31], electrodeposition [32, 33], chemical vapor deposition [34], electrochemical anodic oxidation [35], spray pyrolysis [36], template-assisted [33], chemical bath deposition [37], hydrothermal methods [38, 39], and many others. Among these methods, the hydrothermal method is commonly used for synthesis of nanocrystalline TiO_2 as it offers the flexibility to attain different particle sizes and morphologies. Large-scale synthesis of TiO_2 nanoparticles with large surface area is also achievable with the hydrothermal method, hence its utilization in industrial-scale synthesis TiO_2 powders and thin films. Anderson et al. [40] reported the preparation of nanosize anatase and rutile TiO_2 by hydrothermal treatment of micro emulsions and investigated their activity for photocatalytic wet oxidation of phenol. Well-dispersed TiO_2 nano-crystals were synthesized by Yang et al. [41] using the hydrothermal methods. Rutile TiO_2 nanorods synthesized on a glass substrate at low temperature under hydrothermal condition was reported by Kakiuchi et al. [42]. Maurya et al. [43]. investigated the effect of temperature on rutile TiO_2 using the hydrolysis method and observed that the crystallinity and density of rutile TiO_2 nanocrystals increases by increasing annealing temperature. The effect of repeated annealing temperature on the TiO_2 thin film and their structural, optical and electrical properties synthesized by dip coating sol–gel method was reported by Pakama et al. [44]. The hydrothermal synthesis of TiO_2 nanocrystals in different basic pHs and their applications in dye sensitized solar cells was reported by Anajafi et al. [45].

Table 1 Process parameters employed during the deposition of TiO_2 thin films

Deposition parameter	Set-I	Set-II
Concentration	50 mM Ti source	50 mM Ti source
Deposition time	**6–24 h**	20 h
Reaction temperature	150 °C	150 °C
Annealing temperature	500 °C	**300–600 °C**

The boldface text indicates the parameters varied in the set I and set II of experiments

In the present work, synthesis of nano-structured TiO_2 thin films was carried out by hydrothermal technique, wherein the influence of different deposition parameters such as growth time, reaction temperature, and the film annealing temperature on the optical, structural and morphological properties have been investigated. The optical, morphological and structural characteristics of the synthesized TiO_2 thin films are studied by using various characterization methods such as X-ray diffraction (XRD), Raman spectroscopy, scanning electron microscopy (SEM) and UV–visible spectroscopy. The goal of the present work is to understand the correlation between the deposition parameters (reaction time and annealing temperature) and the growth mechanism of TiO_2 thin films. The

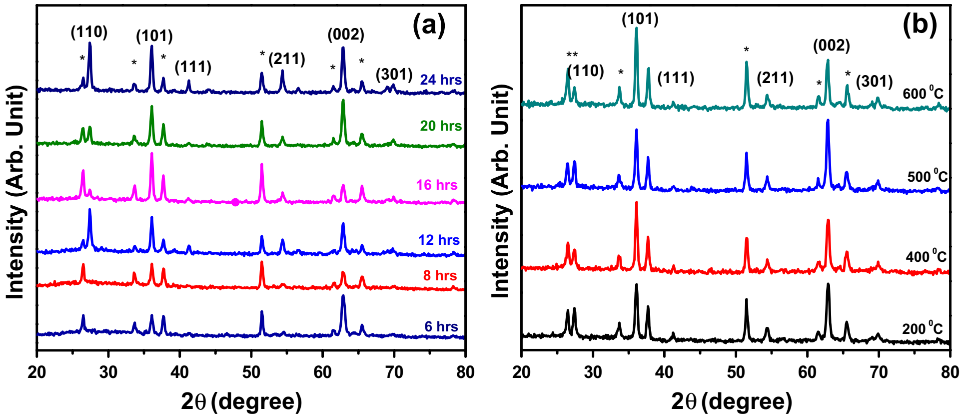

Fig. 2 X-ray diffraction patterns of TiO_2 thin films deposited at **a** different reaction times (6 h, 8 h, 12 h, 16 h, 20 h, 24 h) and **b** different annealing temperatures. The asterisk (*) indicate the peaks of the FTO

field-emission properties of the synthesized TiO_2 thin films are investigated and the results corroborated with first-principles density functional theory (DFT) calculations.

2 Experimental and computational details

2.1 Synthesis

All chemicals used in this work were analytical grade and used without further purification and treatment. For the synthesis of TiO_2 thin film, titanium (IV) butoxide (Sigma-Aldrich), hydrochloric acid (HCl), ethanol and distilled water were subjected to hydrothermal treatment. Commercially available FTO glass substrate was used for the growth of TiO_2 thin film. Titanium (IV) butoxide (5 g) was added to 10 ml HCl followed by the addition of 15 ml double distilled water. The resulting complex was then stirred at room temperature for half an hour using magnetic stirrer. The solution then transferred into locally fabricated cylindrical autoclave having dimensions 8 cm × 9 cm × 1 cm (height × diameter × thickness). The detailed structure of autoclave is schematically shown in Fig. 1. The FTO glass substrates were initially cleaned ultrasonically with double distilled water and followed by an acetone wash. Then substrates were put in ethanol solution for about 5 min. The substrates were again cleaned with double distilled water and finally given a nitrogen flush for drying. This cleaning procedure permits good adhesion of film to substrates. Then cleaned glass substrate was immersed in the solution in autoclave. After the addition of the reaction complexes and substrates, the autoclave was sealed tightly and placed in an oven at 150 °C for different reaction times ranging from 6 to 24 h for the set-I samples. The autoclave was allowed to cool naturally to room temperature. After cooling the film was taken out from autoclave and annealed at different temperature as shown in Table 1 for an hour. Two sets of films were deposited: in the first set, the TiO_2 thin films were deposited at different reaction times i.e. from 6 to 24 h by keeping other parameters (concentration of the solution, deposition temperature, and annealing temperature) constant, whereas in set-II samples, the depositions was carried out with reaction time of 20 h for all the samples, with the annealing temperature varied from 300 to 600 °C and other deposition parameters were kept constant as listed in Table 1.

2.2 Material characterization

The average crystallite size, lattice parameter, inter planner distance, and phase identification of the deposited TiO_2 thin films were carried out using X-ray diffraction (XRD) pattern recorded using (Bruker D8 Advance machine, Germany) diffractometer with Cu Kα ($\lambda = 1.5418$ Å) radiation at a grazing angle of 1° and diffraction angle (2θ) ranging from 20° to 80°. Raman spectra were recorded with Raman spectroscope (Jobin–Yvon Horibra LABRAM-HR) in the range of 200–1800 cm^{-1}. The spectrometer has backscattering geometry for detection of Raman spectrum with a resolution of 1 cm^{-1}. The excitation source was 632.8 nm line of He–Ne laser. The possibility of laser induced crystallization in the film was avoided by keeping the power of laser beam at < 5 mW. The optical bandgap of the TiO_2 films was estimated from transmittance and reflectance spectra of the films deposited on commercially available FTO glass substrates and were measured using a JASCO, V-670 UV–visible spectrophotometer in the range of 200–1100 nm. The morphological characteristics of the synthesized thin films are studied by a JEOL JSM-6360-LA and Philips XL-30 scanning electron microscope.

2.3 Computational details

The density functional theory (DFT) calculations were performed using the Vienna Ab initio Simulation Package (VASP) [46, 47], a periodic plane wave DFT code

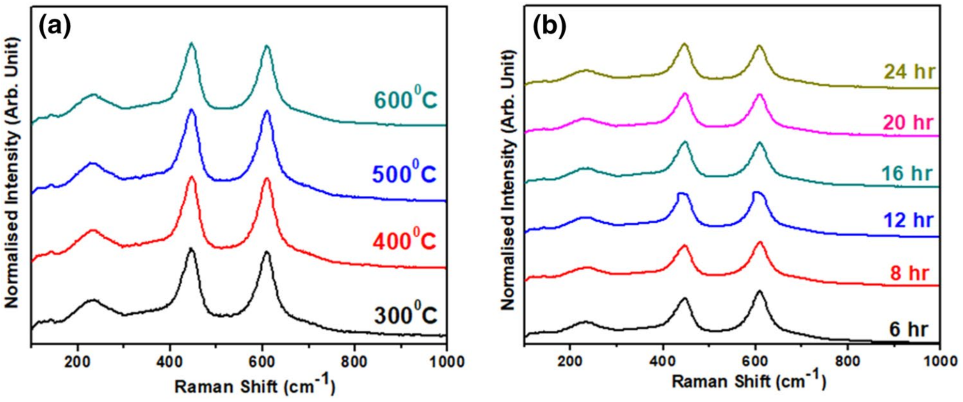

Fig. 3 Raman spectra of TiO_2 films synthesized by hydrothermal technique process **a** at different reaction times **b** at different annealing temperature

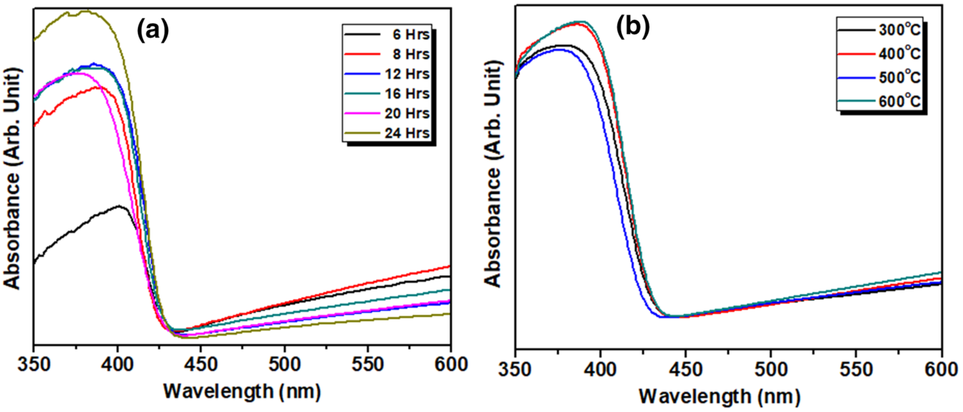

Fig. 4 Optical absorption spectra of TiO_2 thin films synthesized **a** at various reaction times **b** at different annealing temperatures

which includes the interactions between the core and valence elections using the Project Augmented Wave (PAW) method [48]. The calculations were performed using the screened hybrid functional as proposed by Heyd–Scuseria–Ernzerhof (HSE06) [49]. A percentage of the exact non-local Fock exchange ($\alpha = 0.25$) was added to the Perdew, Burke, and Ernzerhof (PBE) functional [50] with a screening of $\omega = 0.11$ bohr^{-1} applied in order to partition the Coulomb potential into long range (LR) and short range (SR) terms. An energy cut-off of 600 eV, and $9 \times 9 \times 3$ and $9 \times 9 \times 1$ Monkhorst–Pack *k*-point mesh [51], was used to sample the sample the Brillouin zone of TiO_2 bulk and (110) surface, respectively. All calculations were deemed to be converged when the forces on all atoms were less than 0.001 eV/Å. Rutile TiO_2 was modelled in the simple-tetragonal structure (Fig. 4a) with space group ($P4_2/mnm$) [52]. The optimized lattice constants were obtained at $a = b = 4.598$Å, $c = 2.953$Å, in close agreement with experimental lattice constants ($a = b = 4.594$ Å and $c = 2.959$Å) [52]. The r-TiO_2(110) surface was created from the optimized bulk material using the METADISE code [53], which ensures the creation of surfaces with zero dipole moment perpendicular to the surface plane [54]. In order to align the energies to the vacuum level, a slab-gap model (slab thickness of 20 Å and vacuum size of 15 Å) was constructed and the corresponding electrostatic potential was averaged along the *c*-direction, using the Macro Density package [55–57], as displayed in Fig. 4(c). The work function (Φ), which is the minimum energy needed to remove an electron from the bulk of a material through a surface to a point outside the material was calculated as $\Phi = V_{vacuum} - E_F$.

3 Results and discussion

The XRD pattern of the set-I and set-II of TiO_2 thin films as described under the synthesis section are depicted in Fig. 2a, b, respectively. The peak position and relative intensity of the TiO_2 phases were confirmed by comparison with standard JCPDS database. The diffraction peaks located at $2\theta = 27.4°$, 36.1°, 41.3°, 54.4°, 62.9° and 69.9° corresponds to the (110), (101), (111), (211), (002) and (301) [58–61] planes of rutile TiO_2 phases (JCPDS no. 076-1939), respectively. No peaks of other phase were detected, thus confirming the successful synthesis of high-purity rutile TiO_2 using hydrothermal method.

The analysis of XRD patterns confirms tetragonal rutile phase of TiO_2 for both the sets. The comparatively broad shoulder located at $2\theta \sim 27.4°$ is observed in all the films,

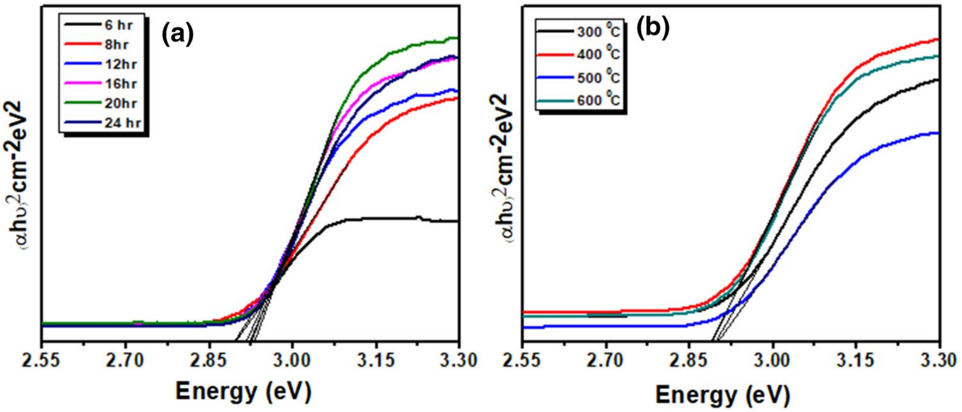

Fig. 5 The $(\alpha h\nu)^2$ versus hν plots (Tauc's plots) of TiO_2 films synthesized **a** at reaction times between 6 and 24 h **b** at process temperature of 150 °C and duration of 20 h, (with annealing at 300 °C, 400 °C, 500 °C, 600 °C)

which is due to the x-ray diffraction occurring from parallel planar layers [62]. The inter planner distance for first order diffraction is 3.26 Å, which is very well matched with the reported values (3.06 Å) in literature [63]. The increased value of inter-planer distance in the present study is attributed to the presence of residual molecules intercalated between the material layers. The estimated lattice constants for the tetragonal structure is a = b=4.6038 Å and *c* = 2.957 Å, which are in good agreement with the reported values in the literature [50]. The average crystallite size of TiO_2 is calculated by measuring FWHM in radian corresponding to (110) peaks by using the Scherer equation $d_{x\text{-}ray} = \frac{0.9\lambda}{\beta\cos(\theta)}$ where, λ is the wavelength of diffracted radiation, θ is the Bragg angle and β is the line width (FWHM) in radians. The crystallite size of TiO_2 was found to be in the range of 23 nm to 34 nm for the film deposited at different deposition time in set I; whereas the maximum crystallite size of 26 nm was observed at 600 °C annealing temperature in set II. In hydrothermal processes, the deposition time and annealing temperature promote the crystallization process. The observed variation in the crystallite size may be due to the non-uniform lattice strain.

The Raman spectroscopy is a resourceful technique used for a fast and non-destructive investigation of a wide-range of Raman active modes of material. Shown in Fig. 3(a, b) are the Raman spectra for both sets of synthesized TiO_2 thin films. Four prominent peaks located at 143.2 cm^{-1}, 235.6 cm^{-1}, 447.1 cm^{-1} and 607.9 cm^{-1} are evident and can be assigned to Raman active mode with the symmetry of E_g for rutile TiO_2 characterized by the tetragonal space group of I41/amd and A_{1g}, B_{1g}, and E_g which is illustrated by the tetragonal space group of P42/mnm for rutile TiO_2 [64–69]. The two prominent maxima peaks located at 447.1 cm^{-1} (E_g) and 607.9 cm^{-1} (A_{1g}) correspond to O–Ti–O bending vibrations and Ti–O stretching vibrations of monocrystalline rutile TiO_2 phase, respectively [37, 67]. The observed prominent Raman shift at 235.6 cm^{-1}, 443 cm^{-1}, 610 cm^{-1}, corresponds to B_{1g}, E_g, A_{1g} active mode of bulk rutile TiO_2, as reported by Begun et al. [70]. Raman shift peak positions shown in the Fig. 3 are in good agreement with those reported in the literature, indicating that synthesized TiO_2 is in the rutile phase. The Raman shift peak at 235 cm^{-1} is attributed to compound vibration peak arising due to multiple phonons scattering process, which is also considered a Raman peak of rutile [71]. There is no observation of Raman active mode for brookite and other organic species impurity phases, which lead us to conclude that the hydrothermal method is the suitable for the synthesis of high-quality rutile TiO_2 thin films for device fabrication.

The optical properties of TiO_2 thin films grown by hydrothermal on FTO glass were investigated from UV–visible spectroscopy. Figure 4 shows the optical absorption spectra of the TiO_2 thin films synthesized using hydrothermal technique at different reaction times and at different annealing temperatures. All the samples synthesized at different reaction times and at different annealing temperatures show sharp absorption edge at 423–430 nm. It also evident from Fig. 4 that the absorption edge shifts towards lower wavelength with increasing reaction times. The shift in the absorption edge towards lower wavelength is attributed to change in the TiO_2 particle size. All the synthesized TiO_2 thin films exhibit very strong and broad UV–visible absorption, similar to the observation by Xie et al. [38, 72] This characteristic is in agreement with the photo-protection function of the TiO_2 films thus formed, making them potential candidates for solar photon capture for photo electrochemical applications. The samples however, show a low absorption above 423 nm, which can be attributed to oxygen vacancy defect formation at the surface boundaries of TiO_2 [73] induced by the higher annealing temperatures. It leads to change of shape of the fundamental absorption edge of the material. As can be seen from Fig. 4, the absorption increases exponentially towards shorter wavelengths, similar to previously reported absorption spectra in the literature [74–76].

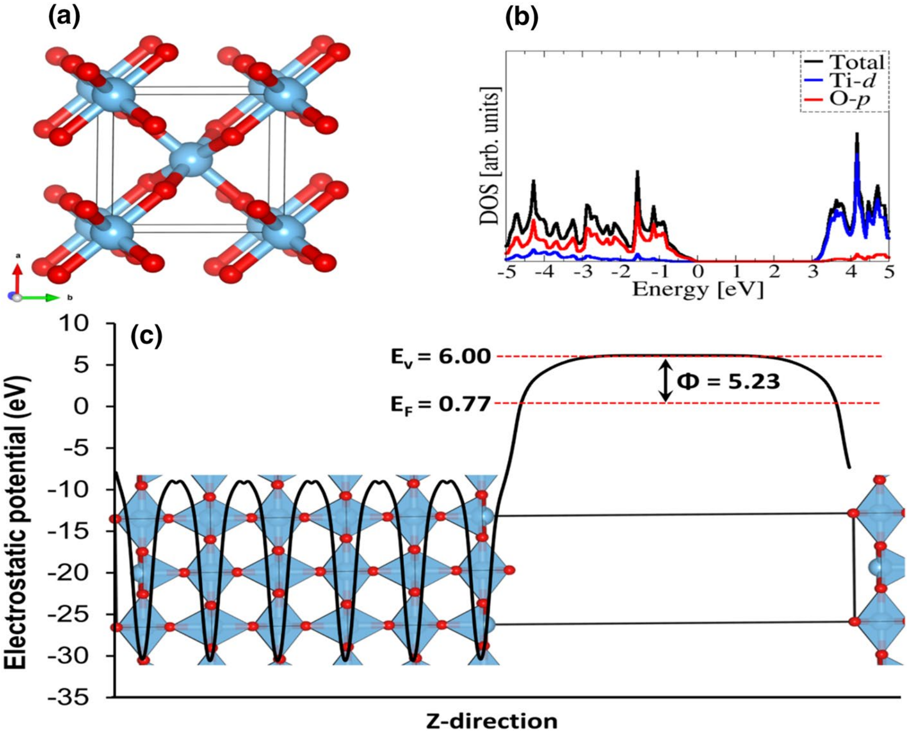

Fig. 6 **a** Crystal structure of the rutile TiO_2; **b** the partial density of states (PDOS) and **c** the electrostatic potential of the (110) surface along coordinate Z considering vacuum as reference energy. E_f, E_v and Φ correspond to the Fermi, vacuum energy and work function of the defined surface. The light blue and red balls correspond to Ti and O atoms, respectively

The optical band gap of the thin films was calculated from the dependence of the absorption coefficient (α) on the photon energy (hν) using Tauc relation: $(\alpha h\nu) = B(h\nu - E_{Tauc})^2$, where B is Tauc's constant which is a characteristic parameter independent of photon energy, α is the absorption coefficient, *h* is the Planck's constant, υ is photon frequency, and E_{Tauc} is the bandgap of the material. The E_{Tauc} estimate can be deduced by plotting $(\alpha E)^2$ versus E and extrapolating the linear portion of the plot to the energy axis. Figure 5 shows the $(\alpha h\nu)^2$ versus (hν) photon energy plots for the TiO_2 thin films prepared at different reaction times and annealing temperatures. The intercept of the plotted tangent gives a good approximation of the band gap energy for this material. The band gap decreases from 2.9 to 2.8 eV when deposition time increases from 6 to 24 h. It is interesting to note that these values are smaller than the reported values of synthetic TiO_2 thin films [77–79]. From the absorption graph, it is confirmed that TiO_2 thin film responds the UV–visible region. The optical absorption of the synthesized sample was found between 423 and 430 nm which corresponds to the band gap of TiO_2 (2.9 eV).

We have employed first-principles DFT calculations to gain insight into the electronic structure and work function of rutile TiO_2 as the field emission properties are strongly dependent on the work function (Φ) of the emitter. Shown in Fig. 6 is the crystal structure of r-TiO_2 with the corresponding electronic partial density of state (PDOS). The badgap is predicted at 3.01 eV, which is good agreement with our experimental measurements and previous DFT calculations [80–82]. An analysis of PDOS reveals that valence band edge is composed mainly of the O-*p* whereas the and conduction band edge is composed mainly of Ti-*d* states, indicating that r-TiO_2 is a O-*p*–Ti-*d* charge transfer semiconductor, which agrees with earlier theoretical predictions [80–82]. The work function was obtained for the most stable (110) surface of r-TiO_2, which was cleaved from the geometrically optimized bulk. A vacuum region of length 15 Å was used in the perpendicular direction to the r-TiO_2 (110) plane to avoid spurious interactions with its own periodic image. Figure 6c shows the structure of the r-TiO_2(110) surface and the corresponding electrostatic potential as a function of coordinate Z (along the c-axis). The work function (Φ) is calculated as the difference between the potential energy of one electron between the Fermi level (E_f) and the vacuum level (E_v). The vacuum level is the potential energy, approaching a nearly constant value in the energy distributions in the vacuum region, which is obtained at 6.00 eV in the present study. The work function of the r-TiO_2(110) surface is predicted at 5.23 eV, in excellent agreement with the values of 5.2–5.5 eV estimated from ultraviolet photoelectron spectroscopy measurements [83–87].

Scanning electron microscopy (SEM) is a convenient method for studying morphology and growth mechanism of the TiO_2 nanorod on the FTO substrates. In the first part, we have investigated the effect of deposition time on growth mechanism of TiO_2 nanorods whiles

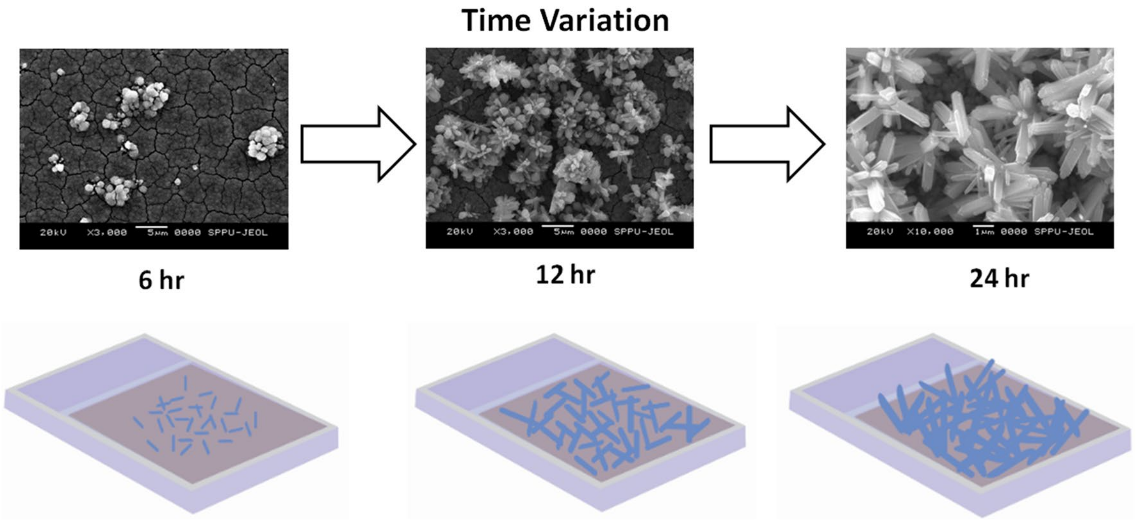

Fig. 7 Scanning electron microscopy (SEM) micrographs of TiO_2 thin films at different reaction times (6, 12, and 24 h**)**

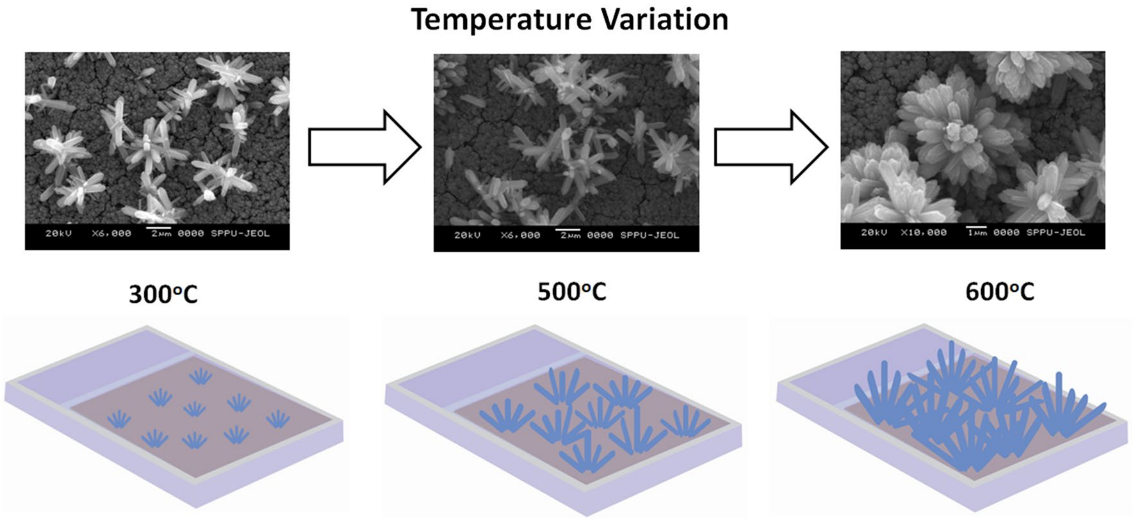

Fig. 8 Scanning electron microscopy (SEM) micrographs of TiO_2 thin films at different annealing temperatures (300 °C, 500 °C, and 600 °C)

keeping other deposition parameters constant. Shown in Fig. 7 are the SEM images of TiO_2 films at different reaction time. It is clear from the SEM images that an increase in the reaction time leads to enhancement in the growth of TiO_2 nanorods. The TiO_2 nanorods started to grow on FTO substrate at the initial reaction time (6 h), which increased in density after 12 h and at 24 h reaction time, the growth of the TiO_2 nanorods covers almost the entire surface areas of the FTO substrate. Shown below each SEM image is the schematic of the nature of the growth process, revealing the growth initiation at 6 h, increased density and random growth after 12 h, and nearly full coverage of TiO_2 nanorods on the FTO substrate at 24 h. Although there is clear evidence of enhanced growth of TiO_2 nanorods with increasing reaction times, we could not control preferential growth orientations of TiO_2 nanorods on FTO substrate in hydrothermal synthesis. In the second part, we have focused on the annealing temperature after synthesis of TiO_2 nanorods in the hydrothermal method. The Fig. 8 shows images of TiO_2 nanorods at different annealing temperatures. We observed clear difference in the growth process of the TiO_2 nanorods at annealing temperature as 300 °C, 500 °C, and 600 °C. At 300 °C, the TiO_2 nanorod started growing in FTO substrate in spherical microstructures. The initial stage of the growth process was limited by the premature termination of the growth surface, but with increased annealing temperature, the regularly shaped particles were transformed to onset of nano-rod

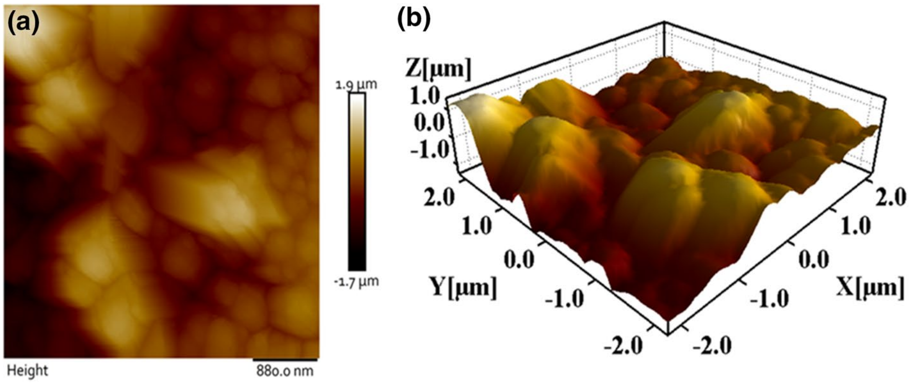

Fig. 9 Atomic force microscopy (AFM) images of TiO_2 thin films at 24 h reaction time, **a** 2-dimensional (2D) AFM image and **b** 3-dimensional (3D) AFM image

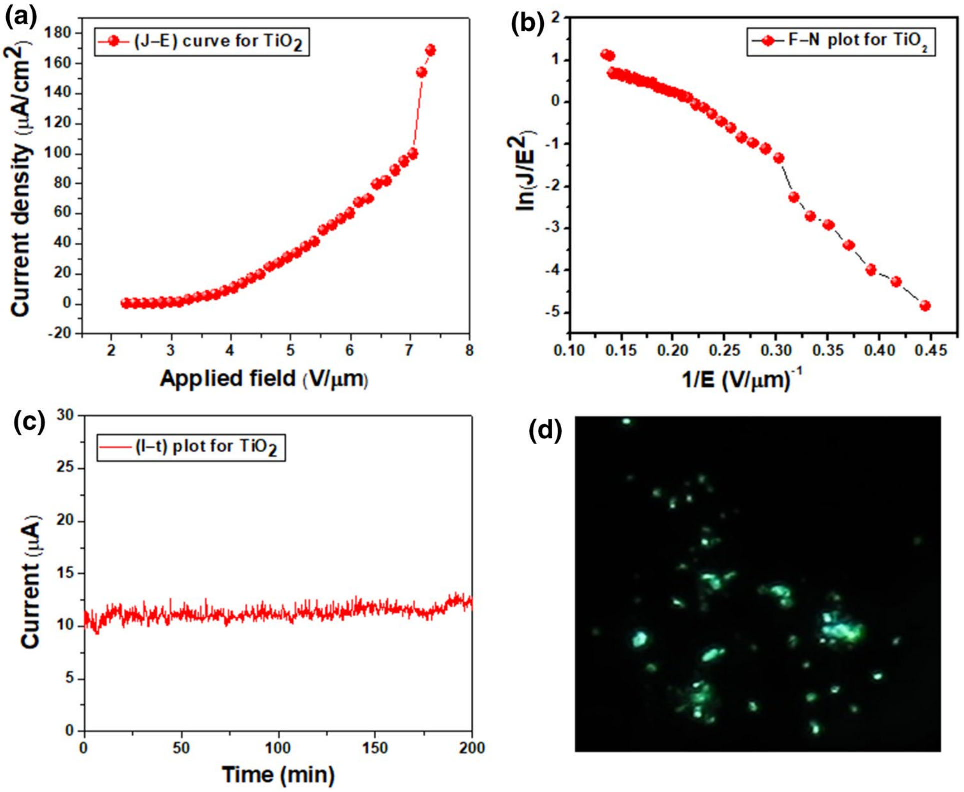

Fig. 10 The field emission properties from TiO_2 nanorods **a** current density (J) versus applied field (E), **b** Fowler–Nordheim (F–N) plot showing non-linear behavior, **c** current stability at 10 µA and **d** photograph of field emission pattern

bunch morphology and further to bunch of nanorods with anchoring on the ITO substrate. Compared to the random growth nature observed with different reaction times as in set I, the growth of the TiO_2 nanorod is pronounced in its random nature with changing annealing temperatures as in set II. The growth of the TiO_2 nanorod on the FTO substrate resembles the growth of a flower in all directions. In schematic diagrams below the SEM images in Fig. 8, we demonstrate how theTiO_2 nanorods grow in uniform shape in a control manner. After the annealing temperature was increased to 500 °C, the TiO_2 nanorod density increased thereby showing the growth of nanorods from a point on the substrate and at 600 °C, the TiO_2 nanorods clearly look like a bunch of flowers. This demonstrates that by varying the annealing temperature we can grow TiO_2 nanorod in a control manner with flower like morphology. The TiO_2 thin films prepared by the hydrothermal technique are without pinholes and provided continuous coverage on the substrate. The uniformly formed rod-like structures of TiO_2 material makes the synthesized thin films better candidates for solar cell (DSSCs) and field emitter arrays applications.

The TiO_2 thin films were characterized using AFM technique and shown in Fig. 9 are the 2-dimensional (2D) and 3-dimensional (3D) AFM images of the TiO_2 thin film at 24 h reaction time. The average roughness and root mean square (RMS) roughness for TiO_2 thin film estimated at 418 nm and 518 nm, respectively.

The pointed nanorod-likeTiO_2 structures are fascinating structures and may be suitable for several applications including as field emitter arrays. We have thus investigated the field emission properties of the TiO_2 nanorods as shown in Fig. 10: (a) current density (J) versus applied field (E), (b) F–N plot, (c) current stability at 10 µA, and (d) photograph of field emission pattern. The current density (J) is defined J = I/A, where I is the emission current and A is the area of emitter. The applied field (E) is defined as E = V/d, where V is the applied voltage, and *d* is the separation between the anode and cathode. According Fowler–Nordheim (F–N) theory, in J–E plot, the emission current from surface of emitter varies as exponentially [88]. TiO_2 nanorods J–E plot showing exponential function. The electron emission quantum tunneling turn on and threshold field were found to be 4.06 and 7.06 V/µm at emission current densities of 10 and 100 µA/cm^2 respectively of TiO_2 nanorods. These values suggest that better turn on field of TiO_2 nanorods are recorded as compared to the ones reported in literature [89–91]. We have obtained the maximum current density of the TiO_2 nanorods to be 168 µA/cm^2 at an applied field of 7.35 V/µm. The F–N plot of TiO_2 nanorods defined by ln(J/E^2) versus 1/E (Fig. 10(b)) shows a non-linear behavior, which is consistent with the semiconductors nature of the TiO_2 emitter. The emission current stability is very important for practical applications as cold cathode. The emission current (I) versus time (t) plot of the TiO_2 nanorods at 10 µA remained fairly stable for more than 3 h as shown Fig. 10c. The observed fluctuations and spikes in emission current may be due to the adsorption or desorption of residual gas atoms/molecules on the surface of TiO_2 nanorod emitter in the presence of applied field. The field emission of TiO_2 nanorods patterns is shown Fig. 10d with the tiny bright spots representing electron emission from protruding sites of TiO_2 nanorods on the fluorescent screen as electron collector.

4 Conclusion

Large-area, very dense, and pin-hole free TiO_2 nanorod thin films were successfully synthesized by a simple and cost effective hydrothermal method. The effect of reaction times and annealing temperatures on the growth mechanisms (size and shape) of the TiO_2 nanorods was systematically studied. The TiO_2 nanorods are demonstrated to grow randomly on the FTO substrate with changing reaction times but grow uniformly in a flower-like pattern with increasing annealing temperature. Recorded X-ray diffraction patterns, UV–VIS spectra, and Atomic force microscope images showed that the crystallinity in TiO_2 thin films is significantly affected by increasing annealing temperature. The optical properties investigated experimentally and further corroborated with first-principles density functional theory calculations show the TiO_2 thin films have high absorption coefficient and a direct bandgap in the range 2.8–3.0 eV, which is slightly smaller than the bandgap of bulk rutile TiO_2. The TiO_2 nanorods exhibit moderate field emission properties and have turn on field of 7.35 V/µm and good field emission stability. These results indicate that TiO_2 nanorods thin films may be promising candidates for applications in electron-emitting nano devices.

Acknowledgements N. Y. D. acknowledges the UK Engineering and Physical Sciences Research Council (EPSRC) for funding (Grant No. EP/S001395/1). This work has also used the computational facilities of the Advanced Research Computing at Cardiff (ARCCA) Division, Cardiff University, and HPC Wales. The author A. M. F. acknowledges Exide Industries Limited for establishment and use of facilities at EXIDE-SPPU Centre of Excellence in Energy Storage on Savitribai Phule Pune University Campus.

Compliance with ethical standards

Conflict of interest On behalf of all authors, the corresponding author states that there is no conflict of interest.

References

1. Mao SS, Chen X (2007) Selected nanotechnologies for renewable energy applications. Int J Energy Res 31:619–636. https://doi.org/10.1002/er.1283
2. Mor GK, Varghese OK, Paulose M, Shankar K, Grimes CA (2006) A review on highly ordered, vertically oriented TiO_2 nanotube arrays: Fabrication, material properties, and solar energy applications. Sol Energy Mater Sol Cells 90:2011–2075. https://doi.org/10.1016/j.solmat.2006.04.007
3. Mills A, Hunte SL (1997) An overview of semiconductor photocatalysis. J Photochem Photobiol A 108:1–35. https://doi.org/10.1016/S1010-6030(97)00118-4
4. Linsebigler AL, Lu G, Yates JT Jr (1995) Photocatalysis on TiO_n surfaces: principles, mechanisms, and selected results. Chem Rev 95:735–758. https://doi.org/10.1021/cr00035a013
5. Ollis DF, Pelizzetti E, Serpone N (1991) Photocatalyzed distruction of water contaminants. Environ Sci Technol 25(9):1522–1529. https://doi.org/10.1021/es00021a001
6. Herzog C, Belaidi A, Ogacho A, Dittrich T (2009) Inorganic solid state solar cell with ultra-thin nanocomposite absorber based on nanoporous TiO_2 and In2S3. Energy Environ Sci 2:962–964. https://doi.org/10.1039/B905897D
7. Ambade SB, Ambade RB, Mane RS, Lee GW, Shaikh SF, Patil SA, Joo O, Han SH, Lee SH (2013) Low temperature chemically synthesized rutile TiO_2 photoanodes with high electron lifetime for organic dye-sensitized solar cells. Chem Commun 49:2921–2923. https://doi.org/10.1039/c3cc00310h

8. Yaoguang Y, Gang C, Yansong Z, Zhonghui H (2015) Recent advances in rare-earth elements modification of inorganic semiconductor based photocatalysts for efficient solar energy conversion: a review. J Rare Earths 33:5. https://doi.org/10.1016/S1002-0721(14)60440-3
9. Mali SS, Devan RS, Ma Y, Betty CA, Bhosale PN, Panmand RP, Kale BB, Jadkar SR, Patil PS, Kim JH, Hong CK (2013) Effective light harvesting in CdS nanoparticle-sensitized rutile TiO_2 microspheres. Electrochim Acta 90:666–672. https://doi.org/10.1016/j.electacta.2012.12.017
10. Yin X, Que W, Fei D, Xie H, He Z (2013) Effect of TiO_2 shell layer prepared by wet-chemical method on the photovoltaic performance of ZnO nanowires arrays-based quantum dot sensitized solar cells. Electrochim Acta 99:204–210. https://doi.org/10.1016/j.electacta.2013.03.110
11. Tang J, Durrant JR, Klug DR (2008) Mechanism of photocatalytic water splitting in TiO_2. Reaction of water with photoholes, importance of charge carrier dynamics, and evidence for four-hole chemistry. J Am Chem Soc 130:13885–13891. https://doi.org/10.1021/ja8034637
12. Rasalingam S, Peng R, Koodali RT (2014) Removal of hazardous pollutants from wastewaters: applications of TiO_2–SiO_2 mixed oxide materials. J Nanomater 10:42. https://doi.org/10.1155/2014/617405
13. Zhu RR, Wang WR, Sun XY, Liu H, Wang SL (2010) Enzyme activity inhibition and secondary structure disruption of nano-TiO_2 on pepsin. Toxicol In Vitro 24:1639–1647. https://doi.org/10.1016/j.tiv.2010.06.002
14. Demetrescu I, Pirvu C, Mitran V (2010) Effect of nano-topographical features of Ti/TiO_2 electrode surface on cell response and electrochemical stability in artificial saliva. Bioelectrochemistry 79:122–129. https://doi.org/10.1016/j.bioelechem.2010.02.001
15. Anpo M, Kamat PV (2010) Environmentally benign photocatalysts: applications of titanium oxide-based materials. Springer, New York
16. Ramadoss A, Kim SJ (2013) Vertically aligned TiO_2 nanorod arrays for electrochemical supercapacitor. J Alloys Compd 561:262–267. https://doi.org/10.1016/j.jallcom.2013.02.015
17. Yue L, Zhang X (2009) Structural characterization and photocatalytic behaviors of doped CeO_2 nanoparticles. J Alloys Compd 475:702–705. https://doi.org/10.1016/j.jallcom.2008.07.096
18. Dubal DP, Dhawale DS, More AM, Lokhande CD (2011) Synthesis and characterization of photosensitive TiO_2 nanorods by controlled precipitation route. J Mater Sci 46:2288–2293. https://doi.org/10.1007/s10853-010-5070-7
19. Madhugiri S, Sun B, Smirniotis PG, Ferraris JP, Balkus KJ Jr (2004) Electrospun mesoporous titanium dioxide fibers. Microporous Mesoporous Mater 69:77–83. https://doi.org/10.1016/j.micromeso.2003.12.023
20. Calleja G, Serrano DP, Sanz R, Pizarro P, Garcia A (2004) Study on the synthesis of high-surface-area mesoporous TiO_2 in the presence of nonionic surfactants. Ind Eng Chem Res 43:2485–2492. https://doi.org/10.1021/ie030646a
21. Pratsinis SE (1998) Flame aerosol synthesis of ceramic powders. Prog Energy Combust Sci 24:197–219. https://doi.org/10.1016/S0360-1285(97)00028-2
22. Mendoza-Anaya D, Salas P, Chavez CA, Pérez-Hernández R (2003) Microstructural characterization and morphology of TiO_2 for thermoluminescent applications. Rev Mex Fis 1(50):12–16
23. Bakardjieva S, Stengl V, Szatmary L, Subrt J, Lukac J, Murafa N, Niznansky D, Cizek K, Jirkovsky J, Petrova N (2006) Transformation of brookite-type TiO_2 nanocrystals to rutile: correlation between microstructure and photoactivity. J Mater Chem 16:1709–1716. https://doi.org/10.1039/B514632A
24. Jun Y, Casula MF, Sim JH, Kim SY, Cheon J, Alivisatos AP (2003) Surfactant-assisted elimination of a high energy facet as a means of controlling the shapes of TiO_2 nanocrystals. J Am Chem Soc 125:15981–15985. https://doi.org/10.1021/ja0369515
25. Cozzoli PD, Kornowski A, Weller H (2003) Low-temperature synthesis of soluble and processable organic-capped anatase TiO_2 nanorods. J Am Chem Soc 125:14539–14548. https://doi.org/10.1021/ja036505h
26. Wicaksana D, Kobayashi A, Kinbara A (1992) Process effects on structural properties of $Ti0_2$ thin films by reactive sputtering. J Vac Sci Technol A 10:4. https://doi.org/10.1116/1.578269
27. Wilson GJ, Matijasevich AS, Mitchell DRG, Schulz JC, Will GD (2006) Modification of TiO_2 for enhanced surface properties: finite Ostwald ripening by a microwave hydrothermal process. Langmuir 22:2016–2027. https://doi.org/10.1021/la052716j
28. Zhang Q, Gao L (2003) Preparation of oxide nanocrystals with tunable morphologies by the moderate hydrothermal method: insights from rutile TiO_2. Langmuir 19:967–971. https://doi.org/10.1021/la020310q
29. Tian ZR, Voigt JA, Liu J, Mckenzie B, Xu H (2003) Large oriented arrays and continuous films of TiO_2-based nanotubes. J Am Chem Soc 125:12384–12385. https://doi.org/10.1021/ja0369461
30. Lee S, Cho I, Lee JH, Kim DH, Kim DW, Kim JY, Shin H, Lee J, Jung OS, Park N, Kim K, Ko MJ, Hong KS (2010) Two-step sol–gel method-based TiO_2 nanoparticles with uniform morphology and size for efficient photo-energy conversion devices. Chem Mater 22:1958–1965. https://doi.org/10.1021/cm902842k
31. Cameron MA, Gartland IP, Smith JA, Diaz SF, George SM (2000) Atomic layer deposition of SiO_2 and TiO_2 in alumina tubular membranes: pore reduction and effect of surface species on gas transport. Langmuir 16:7435–7444. https://doi.org/10.1021/la9916981
32. Yu I, Yu X (2008) Hydrothermal synthesis and photocatalytic activity of zinc oxide hollow spheres. Environ Sci Technol 42:4902–4907. https://doi.org/10.1021/es800036n
33. Endrődi B, Kecsenovity E, Rajeshwar K, Janáky C (2018) One-step electrodeposition of nanocrystalline TiO_2 films with enhanced photoelectrochemical performance and charge storage. ACS Appl. Energy Mater 1:851–858. https://doi.org/10.1021/acsaem.7b00289
34. Pradhan SK, Reucroft PJ, Yang F, Dozier A (2003) Growth of TiO_2 nanorods by metalorganic chemical vapor deposition. J Cryst Growth 256:83–88. https://doi.org/10.1016/S0022-0248(03)01339-3
35. Yu J, Su Y, Cheng B (2007) Template-free fabrication and enhanced photocatalytic activity of hierarchical macro-/mesoporous titania. Adv Funct Mater 17:1984–1990. https://doi.org/10.1002/adfm.200600933
36. Aji BB, Shih SJ, Pradita T (2017) Controlled crystal phase of TiO_2 by spray pyrolysis method. J Phys Conf Ser 817:012021. https://doi.org/10.1088/1742-6596/817/1/012021
37. Mayabadi AH, Waman VS, Kamble MM, Ghosh SS, Gabhale BB, Rondiya SR, Rokade AV, Khadtare SS, Sathe VG, Pathan HM, Gosavi SW, Jadkar SR (2014) Evolution of structural and optical properties of rutile TiO_2 thin films synthesized at room temperature by chemical bath deposition method. J Phys Chem Solids 75:182–187. https://doi.org/10.1016/j.jpcs.2013.09.008
38. Mali SS, Betty CA, Bhosale PN, Patil PS (2011) Hydrothermal synthesis of rutile TiO_2 with hierarchical microspheres and their characterization. CrystEngComm 13:6349–6351. https://doi.org/10.1039/C1CE05928A
39. Shinde DB, Jagadale SK, Mane RK, Mane RM, Ghanwat VB, Khot KV, Mali SS, Hong CK, Bhosale PN (2015) Time dependent facile hydrothermal synthesis of TiO_2 nanorods and their photoelectrochemical applications. J Nanomed Nanotechnol S7:2157–7439. https://doi.org/10.4172/2157-7439.S7-004
40. Andersson M, Oesterlund L, Ljungstrom S, Palmqvist A (2002) Preparation of nanosize anatase and rutile TiO_2 by hydrothermal

treatment of microemulsions and their activity for photocatalytic wet oxidation of phenol. J Phys Chem B 106(41):10674–10679. https://doi.org/10.1021/jp025715y
41. Yang J, Mei S, Ferreira JMF (2002) Hydrothermal synthesis of well-dispersed TiO_2 nano-crystals. J Mater Res 17:2197–2200. https://doi.org/10.1557/JMR.2002.0323
42. Kakiuchi K, Hosono E, Imai H, Kimura T, Fujihara S (2006) {1 1 1}-faceting of low-temperature processed rutile TiO_2 rods. J Cryst Growth 293:541–545. https://doi.org/10.1016/j.jcrysgro.2006.06.004
43. Maurya A, Chauhan P, Mishra SK, Srivastav RK (2011) Structural, optical and charge transport study of rutile TiO_2 nanocrystals at two calcination temperatures. J. Alloys Compd 509:8433–8440. https://doi.org/10.1016/j.jallcom.2011.05.108
44. Pakma O, Serin N, Serin T (2009) The effect of repeated annealing temperature on the structural, optical, and electrical properties of TiO_2 thin films prepared by dip-coating sol–gel method. J Mater Sci 44:401–407. https://doi.org/10.1007/s10853-008-3145-5
45. Anajafi Z, Marandi M, Taghavinia N (2015) Hydrothermal synthesis of TiO_2 nanocrystals in different basic pHs and their applications in dye sensitized solar cells. Physica E 70:113–120. https://doi.org/10.1016/j.physe.2015.02.023
46. Kresse G, Joubert D (1999) From ultrasoft pseudopotentials to the projector augmented-wave method. Phys Rev B 59(3):1758–1775. https://doi.org/10.1103/PhysRevB.59.1758
47. Kresse G, Furthmüller J (1996) Efficient iterative schemes for ab initio total-energy calculations using a plane-wave basis set. Comput Mater Sci 6:15. https://doi.org/10.1103/PhysRevB.54.11169
48. Blöchl PE (1994) Projector augmented-wave method. Phys Rev B 50:17953. https://doi.org/10.1103/PhysRevB.50.17953
49. Krukau AV, Vydrov OA, Izmaylov AF, Scuseria GE (2006) Influence of the exchange screening parameter on the performance of screened hybrid functional. J Chem Phys 125:224106. https://doi.org/10.1063/1.2404663
50. Perdew JP, Burke K, Ernzerhof M (1997) Generalized gradient approximation made simple. Phys Rev Lett 78:1396. https://doi.org/10.1103/PhysRevLett.77.3865
51. Monkhorst HJ, Pack JD (1976) Special points for Brillouin-zone integrations. Phys Rev B 13:5188. https://doi.org/10.1103/PhysRevB.13.5188
52. Abrahams SC, Bernstein JL (1971) Rutile: normal probability plot analysis and accurate measurement of crystal structure. J Chem Phys 55:3206. https://doi.org/10.1063/1.1676569
53. Watson GW, Kelsey ET, de Leeuw NH, Harris DJ, Parker SC (1996) Atomistic simulation of dislocations, surfaces and interfaces in MgO. Chem Soc Faraday Trans 92:433–438. https://doi.org/10.1039/ft9969200433
54. Tasker PW (1979) The stability of ionic crystal surfaces. J Phys C Solid State Phys 12:4977. https://doi.org/10.1088/0022-3719/12/22/036
55. Walsh A, Butler KT (2013) Prediction of electron energies in metal oxides. Acc Chem Res 47:364–372. https://doi.org/10.1021/ar400115x
56. Ganose AM, Butler KT, Walsh A, Scanlon DO (2016) Relativistic electronic structure and band alignment of BiSI and BiSeI: candidate photovoltaic materials. J Mater Chem A 4:2060. https://doi.org/10.1039/C5TA09612J
57. Wu L, Dzade NY, Gao L, Scanlon DO, Öztürk Z, Hollingsworth N, Weckhuysen BM, Hensen EJM, de Leeuw NH, Hofmann JP (2017) Enhanced photoresponse of FeS_2 films: the role of marcasite–pyrite phase junctions. J Adv Mater 28:9602–9607. https://doi.org/10.1002/adma.201602222
58. Sharma A, Karn RK, Pandiyan SK (2014) Synthesis of TiO_2 nanoparticles by sol–gel method and their characterization. J Basic Appl Eng Res 1:1–5
59. Xia X, Peng S, Bao Y, Wang Y, Lei B, Wang Z, Huang Z, Gao Y (2018) Control of interface between anatase TiO_2 nanoparticles and rutile TiO_2 nanorods for efficient photocatalytic H_2 generation. J Power Sources 376:11–17. https://doi.org/10.1016/j.jpowsour.2017.11.067
60. Thamaphat K, Limsuwan P, Ngotawornchai B (2008) Phase characterization of TiO_2 powder by XRD and TEM. Kasetsart J (Nat Sci) 42:357–361
61. Wang Y, Li L, Huang X, Li Q, Li G (2015) Electronic supplementary information (ESI) available for: new understanding of fluorinated TiO_2 (brookite, anatase and rutile) nanoparticles as efficient photocatalytic redox catalysts. RSC Adv 5:34302. https://doi.org/10.1039/c4ra17076h
62. Vorontsov AV, Tsybulya SV (2018) Influence of nanoparticles size on XRD patterns for small monodisperse nanoparticles of Cu^0 and TiO_2 anatase. Ind Eng Chem Res 57:2526–2536. https://doi.org/10.1021/acs.iecr.7b04480
63. Miao L, Jin P, Kaneko K, Terai A, Nabatova-Gabain N, Tanemur S (2003) Preparation and characterization of polycrystalline anatase and rutile TiO_2 thin films by rf magnetron sputtering. Appl Surf Sci 212–213:255–263. https://doi.org/10.1016/S0169-4332(03)00106-5
64. Mazza T, Barborini E, Piseri P, Milani P (2007) Raman spectroscopy characterization of TiO_2 rutile nanocrystals. Phys Rev B 75:045416. https://doi.org/10.1103/PhysRevB.75.045416
65. Ocana M, Garcia-Ramos JV, Serna CJ (1992) Low-temperature nucleation of rutile observed by raman spectroscopy during crystallization of TiO_2. J Am Ceram Soc 75(I71):2010–2012. https://doi.org/10.1111/j.1151-2916.1992.tb07237.x
66. Ohsaka T, Izumi F, Fujiki Y (1978) raman spectrum of anatase, TiO_2. J Raman Spectrosc 7:321–324. https://doi.org/10.1002/jrs.1250070606
67. Ma HL, Yang JY, Dai Y, Zhang YB, Lu B, Ma GH (2007) Raman study of phase transformation of TiO_2 rutile single crystal irradiated by infrared femtosecond laser. Appl Surf Sci 253:7497–7500. https://doi.org/10.1016/j.apsusc.2007.03.047
68. Tamilselvan V, Yuvaraj D, Kumar RR, Rao KN (2012) Growth of rutile TiO_2 nanorods on TiO_2 seed layer deposited by electron beam evaporation. Appl Surf Sci 258:4283–4287. https://doi.org/10.1016/j.apsusc.2011.12.079
69. Meng X, Shin D, Yu SM, Jung JH, Kim HI, Lee HM, Han Y, Bhoraskar V, Yoo J (2011) Growth of hierarchical TiO_2 nanostructures on anatase nanofibers and their application in photocatalytic activity. CrystEngComm 13:3021. https://doi.org/10.1039/C0CE00765J
70. Begun GM, Bamberger CE (1989) Raman spectroscopic observation of laser-induced oxidation of transition-metal borides, carbides, and nitrides. Appl Spectrosc 43:134–138. https://doi.org/10.1366/0003702894201914
71. Yan J, Wu G, Guan N, Li L, Li Z (2013) Understanding the effect of surface/bulk defects onthe photocatalytic activity of TiO_2: anatase versus rutile. Phys Chem Chem Phys 15:10978–10988. https://doi.org/10.1039/c3cp50927c
72. Xie C, Yang S, Shi J, Niu C (2016) Highly Crystallized C-doped mesoporous anatase TiO_2 with visible light photocatalytic activity. Catalysts 6:117. https://doi.org/10.3390/catal6080117
73. Thompson TL, Yates JT Jr (2006) Surface science studies of the photoactivation of TiO_2s new photochemical processes. Chem Rev 106:4428–4453. https://doi.org/10.1021/cr050172k
74. Shirke BS, Korake PV, Hankare PP, Bamane SR, Garadkar KM (2011) Synthesis and characterization of pure anatase TiO_2 nanoparticles. J Mater Sci Mater Electron 22:821–824. https://doi.org/10.1007/s10854-010-0218-4

75. Wang C, Geng A, Guo Y, Jiang S, Qu X, Li L (2006) A novel preparation of three-dimensionally ordered macroporous M/Ti = Zr or Ta) mixed oxide nanoparticles with enhanced photocatalytic activity. J Colloid Interface Sci 301:236–247. https://doi.org/10.1016/j.jcis.2006.05.002
76. Vijayalakshmi R, Rajendran V (2012) Synthesis and characterization of nano-TiO_2 via different methods. Arch Appl Sci Res 4(2):1183–1190
77. Tripathi AK, Singh MK, Mathpal MC, Mishra SK, Agarwal A (2013) Study of structural transformation in TiO_2 nanoparticles and its optical properties. J Alloys Compd 549:114–120. https://doi.org/10.1016/j.jallcom.2012.09.012
78. Tripathi AK, Mathpal MC, Kumar P, Singh MK, Mishra SK, Srivastava RK, Chung JS, Verma G, Ahmad MM, Agarwal A (2014) Synthesis based structural and optical behavior of anatase TiO_2 nanoparticles. Mater Sci Semicond Process 23:136–143. https://doi.org/10.1016/j.mssp.2014.02.041
79. Kawahara T, Ozawa T, Iwasaki M, Tada H, Ito S (2003) Photo-catalytic activity of rutile–anatase coupled TiO_2 particles prepared. J Colloid Interface Sci 267:377–381. https://doi.org/10.1016/S0021-9797(03)00755-0
80. Scanlon DO, Dunnill CW, Buckeridge J, Shevlin SA, Logsdail AJ, Woodley SM, Catlow CRA, Powell MJ, Palgrave RG, Parkin IP, Watson GW, Keal TW, Sherwood P, Walsh A, Sokol AA (2013) Band alignment of rutile and anatase TiO_2. Nat Mater 12:798–801. https://doi.org/10.1038/nmat3697
81. Pfeifer V, Erhart P, Li S, Rachut K, Morasch J, Brötz J, Reckers P, Mayer T, Rühle S, Zaban A, Seró IM, Bisquert J, Jaegermann W, Klein A (2013) Energy band alignment between anatase and rutile TiO_2. J Phys Chem Lett 4(23):4182–4187. https://doi.org/10.1021/jz402165b
82. Pascual J, Camassel J, Mathieu H (1978) Fine structure in the intrinsic absorption edge of TiO_2. Phys Rev B 18:5606–5614. https://doi.org/10.1103/PhysRevB.18.5606
83. Borodin A, Reichling M (2011) Characterizing TiO_2(110) surface states by their work function. Phys Chem Chem Phys 13:15442–15447. https://doi.org/10.1039/c0cp02835e
84. Chung YW, Lo WJ, Somorjai GA (1977) Low energy electron diffraction and electron spectroscopy studies of the clean (110) and (100) titanium dioxide (rutile) crystal surfaces. Surf Sci 64:588. https://doi.org/10.1016/0039-6028(77)90064-4
85. Onishi H, Aruga T, Egawa C, Iwasawa Y (1988) Adsorption of CH_3OH, HCOOH and SO_2 on TiO_2 (110) and stepped TiO_2 (441) surfaces. Surf Sci 193(1–2):33–46. https://doi.org/10.1016/0039-6028(88)90321-4
86. Onda K, Li B, Petek H (2004) Two-photon photoemission spectroscopy of TiO_2(110) surfaces modified by defects and O_2 or H_2O adsorbates. Phys Rev B 70:045415. https://doi.org/10.1103/PhysRevB.70.045415
87. Schierbaum K, Fischer S, Wincott P, Hardman P, Dhanak V, Jones G, Thornton G (1997) Electronic structure of Pt overlayers on (1 × 3) reconstructed TiO_2(100) surfaces. Surf Sci 391:196–203. https://doi.org/10.1016/S0039-6028(97)00483-4
88. Zubair M, Ang YS, Ang LK (2018) Fractional Fowler–Nordheim law for field emission from rough surface with nonparabolic energy dispersion. IEEE Trans Electron Devices 65:2089–2095. https://doi.org/10.1109/TED.2017.2786020
89. Chavan PG, Shende SV, Joag DS, More MA (2011) Photo-enhanced field emission study of TiO_2 nanotubes array. Ultramicroscopy 111:415–420. https://doi.org/10.1016/j.ultramic.2010.11.001
90. Xiang B, Zhang Y, Wang Z, Luo XH, Zhu YW, Zhang HZ, Yu DP (2005) Field-emission properties of TiO_2 nanowire arrays. J Phys D Appl Phys 38:1152–1155. https://doi.org/10.1088/0022-3727/38/8/009
91. Didwal PN, Chikate PR, Bankar PK, More MA, Devan RS (2019) Intense field electron emission source designed from large area array of dense rutile TiO_2 nanopillars. J Mater Sci Mater Electron 30:2935–2941. https://doi.org/10.1007/s10854-018-00570-9